

ORIGINAL ARTICLE

Open Access



Numerical Simulation and Experimental Verification of the Stiffness and Stability of Thrust Pad Aerostatic Bearings

Hai-Long Cui*, Yang Wang, Bao-Rui Wang, Hong Yang and Huan Xia

Abstract

Many researchers concentrate on improving the stiffness and stability of aerostatic bearings, however the contradiction between stiffness and stability is still existed. Therefore, orifice, multiple, and porous restrictors are designed to illustrate the influence of restrictor characteristics on the stability and stiffness of the aerostatic circular pad bearings. Because both the stiffness and stability of aerostatic bearings are determined by the internal pressure distribution, the full Navier-Stokes (N-S) equations are applied to solve internal pressure distribution in bearing film by using computational fluid dynamics (CFD) method. Simulation results present that the stiffness and stability of aerostatic circular pad bearings are influenced significantly by geometrical and material parameters, such as film thickness, orifice diameters, and viscous resistance coefficient. Verified by the experimental data, the micro vibration of orifice restrictor is almost the same as multiple restrictors with amplitude of 0.02 m/s^2 , but it is much stronger than the porous restrictors with acceleration of 0.006 m/s^2 . The optimal stiffness of multiple restrictors increased by 46%, compared to only $30.2 \text{ N}/\mu\text{m}$ of orifice restrictor, and the porous restrictors had obvious advantage in the small film thickness less than $6 \mu\text{m}$ where the optimal stiffness increased to $38.3 \text{ N}/\mu\text{m}$. The numerical and experimental results provide guidance for improving the stiffness and stability of aerostatic bearings.

Keywords: Aerostatic bearings, CFD, Restrictor characteristics, Stability and stiffness

1 Introduction

Aerostatic bearings, which are nearly frictionless, require low driving power and possess high accuracy of movement, have been widely used in ultra-precision machine tools. With regard to the static and dynamic characteristics of aerostatic bearings, stiffness and stability play a key role in achieving nanometer-level motion precision. Huo et al. [1] pointed out that ultra-precision micro milling machine required a high stiffness aerostatic bearings to maintain high accuracy in the presence of large cutting forces. Gao et al. [2] indicated that the stiffness and vibration of high-speed aerostatic spindles were essential for ultra-precision micro-milling machine tools. Yuan et al. [3] presented that the manufacturing precision of ultra-precision machine tool relied on the stiffness and stability

of the aerostatic bearings. Wang et al. [4] demonstrated bearing vibration can have a significant influence on the machining precision of the high-precision optical components in ultra-precision diamond turning. An et al. [5] studied the influence of stability of aerostatic bearing spindles on the machining precision of ultra-precision fly-cutting machines used for processing large diameter optical components.

Among the various restrictor types found in aerostatic bearings, the orifice-type restrictor has attracted considerable attention due to its simple design and low manufacturing cost. Gao et al. [6] conducted the influence the chamber shape on performance characteristics of aerostatic thrust bearings, and found that the pressure depression, gas vortices, and the turbulent intensity which were all weakened with decreasing air film thickness. Li et al. [7] described the study on the performance of aerostatic thrust bearing with pocketed orifice-type restrictor, and presented that ignoring the influences of

*Correspondence: cuihailong61@foxmail.com
Institute of Machinery Manufacturing Technology, China Academy of Engineering Physics, Mianyang 621900, China

orifice length on the bearing's performance resulted in large errors. Renn et al. [8] focused on the mass flow-rate characteristic through an orifice-type restrictor in aerostatic bearings, and showed that the mass flow-rate characteristic through an orifice was different from that through a nozzle.

Over the last few years, published research focuses largely on the stiffness characteristics of aerostatic bearings with orifice restrictors. Cheng et al. [9] gave a selection strategy for the design of externally pressurized journal bearings, and pointed out that the stiffness of aerostatic bearings increased obviously with the growth of supply pressure. Chen et al. [10] investigated the influences of operational conditions and geometric parameters on the stiffness of aerostatic journal bearings, and found that gas-bearing geometries had a significant effect on stiffness. Neves et al. [11] conducted theoretical investigation of the discharge coefficient influence on the stiffness performance of aerostatic journal bearings. Du et al. [12] researched the effects of pressure equalizing groove on the load capacity and stiffness of externally pressurized gas journal bearings.

Various structural designs are used to increase the stiffness of aerostatic bearings. One of these includes rectangular recesses, compared to designs with no recesses, significantly improves stiffness and is superior to spherical recesses [13]. However, increasing the stiffness of aerostatic bearings with orifice restrictors also increases micro vibration. Bhat et al. [14] studied the static and dynamic characteristics of inherently compensated orifice based flat pad air bearing system, and presented that pneumatic hammer instability tended to occur at high pressure. Nishio et al. [15] analyzed the static and dynamic characteristics of aerostatic thrust bearings with small feed holes, and confirmed that aerostatic thrust bearings with small feedholes had larger stiffness and damping coefficient than bearings with compound restrictors. Wang et al. [16] focused on the interaction of shock waves with boundary layer, which caused the instability of aerostatic bearing with orifice restrictor. Xiong et al. [17] studied the mechanism of hydrostatic spindle rotational error motion, and found that increasing of stiffness resulted in the reduction of stability.

Many investigators studies on the mechanism behind micro vibration in aerostatic bearings. Chen et al. [18, 19] demonstrated that micro-vibration was closely related to air vortices that appeared near the air inlet of the aerostatic bearings and that the strength of these air vortices could be represented by a pressure drop from the edge of the vortex to its center. Mohamed and Yoshimoto indicated that a shockwave occurred during the transition from subsonic to supersonic and that the airflow transition between laminar and turbulent flow led to a pressure

drop and recovery in the bearing clearance [20, 21]. To date, there is no suitable method to address the contradictory relationship between stiffness and vibration in aerostatic bearings with orifice restrictors.

To overcome the drawbacks of orifice restrictors, the use of porous restrictors and multiple restrictors are reported. Panzera and Otsu showed that the use of a porous material as the bearing restrictor had the benefit of more uniform pressure distribution over the entire bearing surface, which created higher load capacity, stiffness, damp, and wider stability [22, 23]. Charki et al. [24] found that the stiffness of aerostatic bearings with multiple restrictors could be improved because of the smaller pressure drop near the gas inlet. Published literatures reveal that there are not comprehensive studies considering the influences of different restrictor characteristics on the stiffness and stability of aerostatic bearings. Compared to orifice restrictor, porous restrictors and multiple restrictors were designed to improve the stability and stiffness of aerostatic circular pad bearings in this paper. Taking into account that both the stiffness and the stability of aerostatic bearings were determined by the internal pressure distribution characteristics, the pressure distribution in the bearing clearance of three different restrictors was studied using CFD. The influence of film thickness, orifice diameter, and material parameters on the stiffness and stability of the aerostatic circular pad bearings was also investigated. In addition, the accuracy of the numerical simulation results was verified by the experimental data.

2 Numerical Modeling

2.1 Structures of Restrictors

The basic geometric structures of orifice restrictor, multiple restrictors, and porous restrictors are shown in Figure 1. The pressurized gas flows through the orifice restrictor to the bearing film and leaks from the film edge out to the atmosphere, as shown in Figure 1(a). The pressure chamber of a multiple restrictors is located between the orifice restrictor and the bearing film, as shown in Figure 1(b). The entire upper surface of the bearing film is covered by a porous material, as shown in Figure 1(c).

2.2 Governing Equations

In fluid mechanics, the motion of fluid is governed by the laws of conservation of mass, conservation of momentum and conservation of energy, which can be represented by the N-S equations. The law of conservation of mass, also known as the continuity equation, is given by

$$\frac{\partial \rho}{\partial t} + \frac{\partial(\rho u)}{\partial x} + \frac{\partial(\rho v)}{\partial y} + \frac{\partial(\rho w)}{\partial z} = 0. \quad (1)$$

The divergence can be expressed as

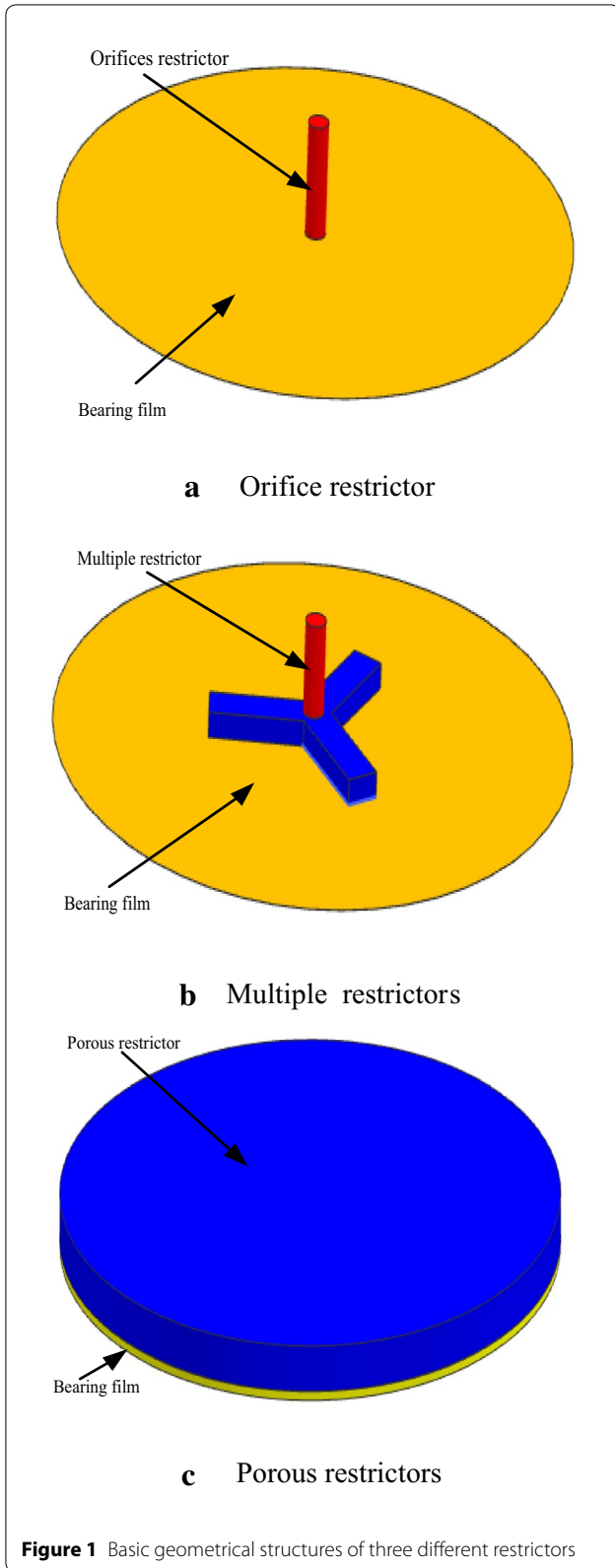


Figure 1 Basic geometrical structures of three different restrictors

$$\frac{\partial \rho}{\partial t} + \text{div}(\rho \mathbf{u}) = 0 \tag{2}$$

where \mathbf{u} is the velocity vector, x , y , and z are the three components of the Cartesian coordinates, u , v , and w are the time-averaged Cartesian velocity components in the three coordinate directions, ρ is the density, and t is time.

According to Newton's second law, the equations for the conservation of momentum in the x , y and z directions are derived as follows:

$$\begin{cases} \frac{\partial(\rho u)}{\partial t} + \text{div}(\rho \mathbf{u}u) = -\frac{\partial p}{\partial x} + \frac{\partial \tau_{xx}}{\partial x} + \frac{\partial \tau_{yx}}{\partial y} + \frac{\partial \tau_{zx}}{\partial z} + F_x, \\ \frac{\partial(\rho v)}{\partial t} + \text{div}(\rho \mathbf{u}v) = -\frac{\partial p}{\partial y} + \frac{\partial \tau_{xy}}{\partial x} + \frac{\partial \tau_{yy}}{\partial y} + \frac{\partial \tau_{zy}}{\partial z} + F_y, \\ \frac{\partial(\rho w)}{\partial t} + \text{div}(\rho \mathbf{u}w) = -\frac{\partial p}{\partial z} + \frac{\partial \tau_{xz}}{\partial x} + \frac{\partial \tau_{yz}}{\partial y} + \frac{\partial \tau_{zz}}{\partial z} + F_z, \end{cases} \tag{3}$$

where p is the pressure in bearing film, and F is the force on the body. For a Newtonian fluid, the viscous stress τ is proportional to the deformation rate of the fluid, given as follows:

$$\begin{cases} \tau_{xx} = 2\mu \frac{\partial u}{\partial x} + \lambda \text{div}(\mathbf{u}); \tau_{xy} = \tau_{yx} = \mu \left(\frac{\partial u}{\partial y} + \frac{\partial v}{\partial x} \right), \\ \tau_{yy} = 2\mu \frac{\partial v}{\partial y} + \lambda \text{div}(\mathbf{u}); \tau_{xz} = \tau_{zx} = \mu \left(\frac{\partial u}{\partial z} + \frac{\partial w}{\partial x} \right), \\ \tau_{zz} = 2\mu \frac{\partial w}{\partial z} + \lambda \text{div}(\mathbf{u}); \tau_{yz} = \tau_{zy} = \mu \left(\frac{\partial v}{\partial z} + \frac{\partial w}{\partial y} \right), \end{cases} \tag{4}$$

Where μ is the dynamic viscosity, and $\lambda = -2/3$.

Based on the first law of thermodynamics, the law of conservation of energy is given by

$$\frac{\partial(\rho T)}{\partial t} + \text{div}(\rho \mathbf{u}T) = \text{div} \left(\frac{k}{c_p} \text{grad}T \right) + S \tag{5}$$

where k is the fluid heat transfer coefficient, c_p is the specific heat capacity, T is the temperature, $\text{grad} T$ is the gradient of the temperature, and S is the viscous dissipation energy.

For aerostatic bearings with orifice restrictor or multiple restrictors, the pressure distribution in the bearing clearance can be obtained by solving Eqs. (2)–(5). For porous aerostatic bearings, viscous loss and inertial loss lead to the pressure drop in the porous material. Based on the Darcy-Forchheimer law, the pressure distribution equation of the porous material can be expressed by

$$\nabla P_i = - \left(\sum_{j=1}^3 D_{ij} \mu u_j + \sum_{j=1}^3 C_{ij} \frac{1}{2} \rho |u| u_j \right) \tag{6}$$

where D_{ij} is the viscous resistance coefficient matrix, and C_{ij} is the inertial resistance coefficient matrix. The laws of conservation of mass and conservation of momentum can be rewritten as

$$\frac{\partial(\gamma\rho)}{\partial t} + \text{div}(\gamma\rho\mathbf{u}) = 0, \tag{7}$$

$$\frac{\partial(\gamma\rho\mathbf{u})}{\partial t} + \text{div}(\gamma\rho\mathbf{u} \times \mathbf{u}) = -\gamma\nabla p \tag{8}$$

where γ is the porosity. The pressure distribution of porous aerostatic bearings can be obtained by solving Eqs. (5)–(8).

2.3 Method of Calculation

The main methods utilized for calculating the flow field characteristics of aerostatic bearings include the finite element method (FEM) [25], the finite difference method (FDM) and CFD method [26]. The Reynolds equation can be solved efficiently by the FEM and FDM. However, because of the large number of assumptions and simplifications required for the Reynolds equation, even if it is supplemented by three-region theory, it is unable to explain the phenomenon of pressure drop and recovery near the gas inlet [27]. For steady flow and a compressible fluid, the microscopic flow characteristics can be effectively captured by the full 3D N-S equation. In this study, FLUENT software, based on the CFD method, was used to solve the N-S equation, and the $k-\epsilon$ model was chosen to calculate the turbulence. The effect of swirl on turbulence is included in the RNG model, which can improve the accuracy for swirling flow near the inlet. Thus, the RNG model was chosen within the $k-\epsilon$ model, and C_1 and C_2 were set to 1.42 and 1.68, respectively.

2.4 Calculation Grids and Boundary Conditions

In many previous studies, the structure of aerostatic circular pad bearings was simplified to the axial symmetric model or the periodic symmetric model [13]. Figure 2 shows the calculation grids and boundary conditions used for orifice restrictor, multiple restrictors, and porous restrictors. In this study, to reduce the scale of computation and to improve computation efficiency, the axial symmetric model was used to analyze the characteristics of aerostatic circular pad bearings with orifice restrictor and porous restrictors, as shown in Figure 2(a), (c), respectively. With regard to the porous restrictors, the interface was defined as the link between the porous region and the gas film region. The periodic symmetric model was chosen for the multiple restrictors, as shown in Figure 2(b), and only one-third of the geometric structure was necessary to perform the calculations. A grid at least four layers thick was required in the direction of the gas film to guarantee convergence. Before calculation, a grid's independence must be tested to ensure the accuracy of the simulation results. The conditions utilized for computation for the three different types of restrictors are listed in Table 1.

3 Experimental Setup

The experimental samples of three types of restrictors are shown in Figure 3. The orifice restrictor, consisting of a copper alloy material, was machined by micro-electrical

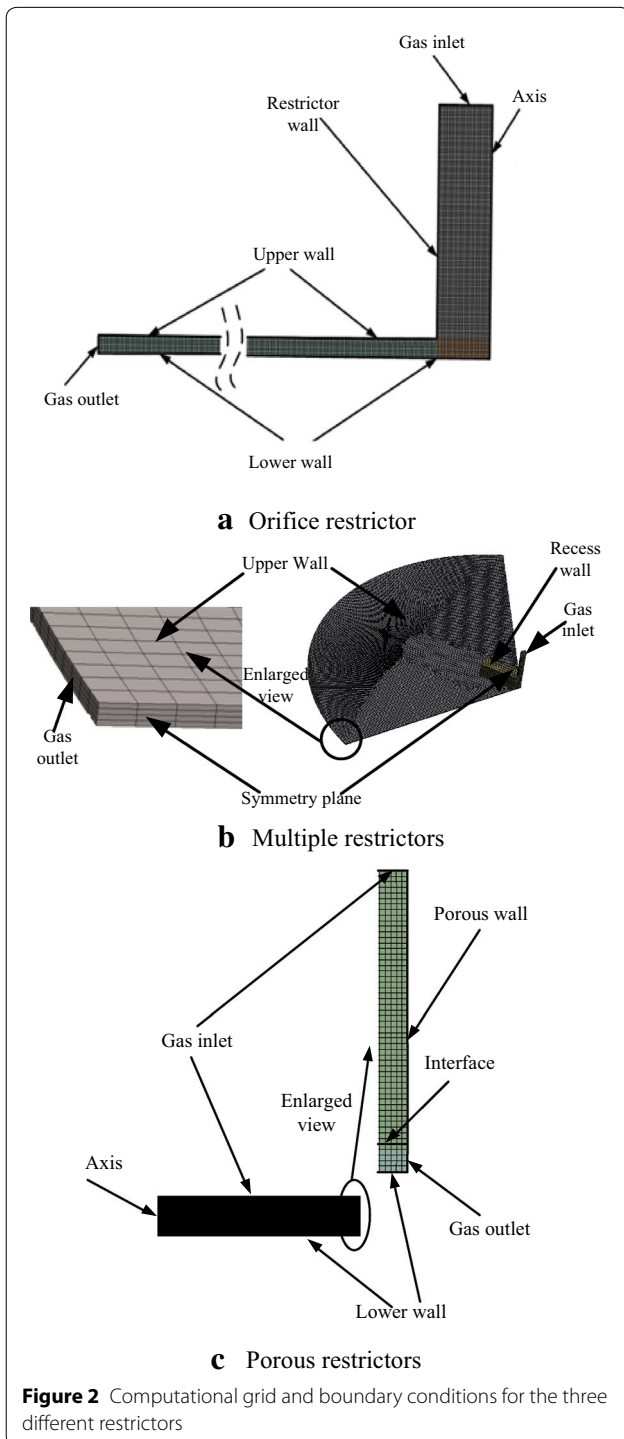


Figure 2 Computational grid and boundary conditions for the three different restrictors

Table 1 Computational conditions of three different restrictors

Design variable	Orifice restrictor	Multiple restrictors	Porous restrictors
Inlet pressure P_{in}/Pa	5	5×10^5	5×10^5
Outlet pressure P_{out}/Pa	0	0	0
Operating pressure P_o/Pa	1×10^5	1×10^5	1×10^5
Gas density $\rho/(\text{kg}/\text{m}^3)$	1.189	1.189	1.189
Dynamic viscosity $\mu/(\text{Ns}/\text{m}^2)$	1.8×10^{-5}	1.8×10^{-5}	1.8×10^{-5}
Bearing diameter D/mm	50	50	50
Orifice diameter d/mm	0.05–0.15	0.05–0.15	–
Groove width w_g/mm	–	0.20	–
Groove depth d_g/mm	–	0.10	–
Groove length l_g/mm	–	1.50	–
Viscous resistance coefficient d_r/m^{-2}	–	–	8×10^{13} – 1.6×10^{14}
Inertia resistance coefficient c_r/m^{-1}	–	–	2.5×10^7
Porosity γ	–	–	0.18

discharge machining (micro-EDM), as shown in Figure 3(a). The multiple restrictors was machined from the aluminum alloy by micro-milling and is shown in Figure 3(b). The porous restrictors, which was composed of graphite materials, was fabricated via cold isostatic pressing (CIP), and is shown in Figure 3(c). The detailed structural and material parameters of the three experimental samples are listed in Table 2.

Figure 4 shows the experimental setup for measuring the stiffness and stability of thrust pad aerostatic bearings. To minimize environmental disturbances, the measuring equipment was located on a vibration isolation platform, and the thrust pad aerostatic bearings were tested on its marble base. A fixed support was used to maintain the position of a load transducer and the aerostatic bearings. Pressurized gas regulated by a valve was channeled into the aerostatic bearings by means of a gas channel in the marble base. A throttle plug was utilized to swap between the different restrictor types. The force applied on the aerostatic bearings could be accurately measured by the load transducer. The change in film thickness was measured by displacement sensors (TESA-TRONIC TT80), which possessed a digital resolution of 10 nm. The displacement sensors were installed in the upper edges of the aerostatic bearings at equal intervals.

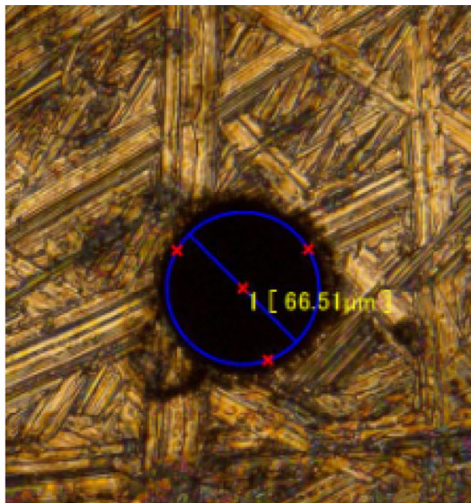
The stability of each aerostatic bearing was measured at the same three positions using acceleration sensors (AD10T), which possessed a sensitivity of 10 mV/g. The value of the acceleration reflects the stability of the aerostatic bearing. During the stability test, the shaft of the aerostatic bearing remained stationary.

4 Results and Discussion

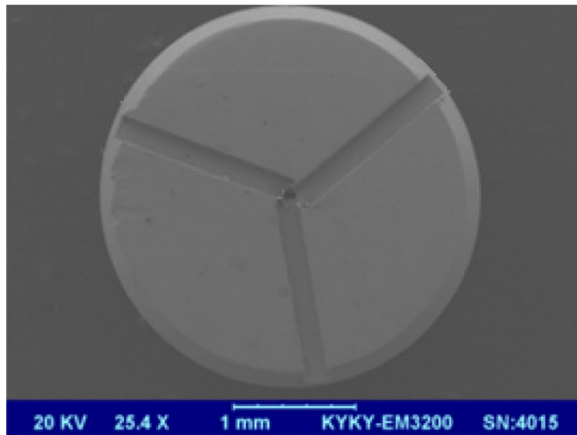
4.1 Numerical Analysis

In this paper, the SIMPLE algorithm, the ideal gas model and the double precision pressure-based solver were selected in the FLUENT software. Based on a film thickness of $h=6 \mu\text{m}$, orifice restrictor diameter of $d=0.1 \text{ mm}$, an operating pressure of 100 kPa, an inlet gas pressure of 500 kPa, and an outlet gas pressure of 0 kPa, a 3D view of the fluid domain pressure distribution was obtained using a post-processing function, as shown in Figure 5. According to the computed pressure distribution of the orifice restrictor, the pressure dropped sharply near the inlet of the restrictor, then decreased smoothly from the inlet to the outlet. The pressure contours of the multiple restrictors showed that the presence of multiple chambers had a significant impact on the ability to maintain a high pressure. The area of the gas film surface at high pressure clearly increased. Figure 5(c) shows the pressure contours of the porous restrictors. In this figure, Section 1 shows the pressure on the upper surface of the porous material, Section 2 represents the two-dimensional (2D) pressure distribution along the center, and Section 3 shows the pressure distribution in the bearing clearance. Based on the pressure distribution of the porous restrictors, it is obvious that the pressure distribution in the bearing clearance is more uniform than that in the orifice restrictor because the surface of the porous material contains countless small holes.

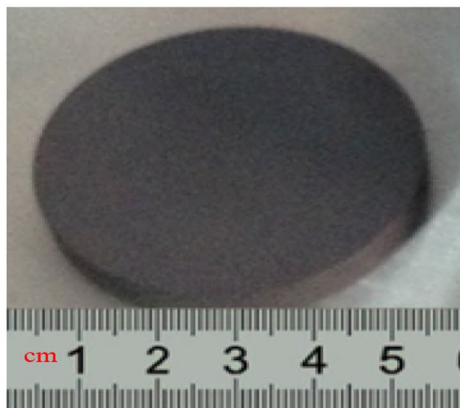
The pressure distribution characteristics in the radial direction of the orifice restrictor with an orifice diameter of 0.10 mm are shown in Figure 6. The phenomenon



a Orifice restrictor



b Multiple restrictors



c Porous restrictors

Figure 3 Experimental samples of the three different restrictor types

of pressure drop and recovery near the gas inlet was accurately captured. In this paper, ΔP is defined as the strength of the pressure drop and recovery phenomenon. It is obvious that ΔP increases from 0 to almost 85 kPa, which means that the aerostatic bearings become unstable with an increase in film thickness. Under the same conditions (film thickness $h=6 \mu\text{m}$), the influence of the restrictor diameter (0.05 mm, 0.10 mm, 0.15 mm) on the pressure distribution characteristics is shown in Figure 7. ΔP increases from 0.18 to 70 kPa as the orifice restrictor diameter decreases, leading to instability of the aerostatic bearings. Many investigators have demonstrated that the instability of aerostatic bearings is closely related to the air vortices that appear near the air inlet of the bearings and that the strength of the air vortices can be represented by the pressure drop between the edge of the vortex and its center. The strength of the air vortices increases as the supply pressure increases. The problem of the stability of the aerostatic bearings cannot be solved effectively by changing the diameter, length or recess shape of the orifice restrictor.

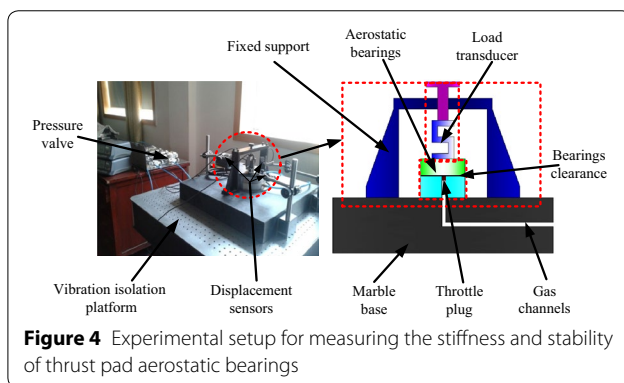
However, compared to the orifice restrictor, the multiple restrictors clearly demonstrated a lower pressure drop, as shown in Figure 8. Therefore, the load capacity and stability of aerostatic bearings with multiple restrictors can be effectively improved, in theory. For the porous restrictors, the pressure distribution characteristics in the radial direction are shown in Figure 9. The phenomenon of pressure drop and recovery near the gas inlet did not occur. The pressure distribution in the bearing clearance was more uniform than in the orifice restrictor and multiple restrictors due to the ubiquitous small holes in the surface of the porous material. Therefore, the porous aerostatic bearing exhibited better stability. Under conditions of subsonic flow, the effect of the viscous resistance coefficient is far more significant than that of the inertial resistance coefficient. Under the conditions of a film thickness of $h=6 \mu\text{m}$ and a supply pressure of 500 kPa, the influence of the viscous resistance coefficient ($0.8 \times 10^{14} \text{ m}^{-2}$, $1.2 \times 10^{14} \text{ m}^{-2}$, $1.6 \times 10^{14} \text{ m}^{-2}$) on the pressure distribution characteristics is also shown in Figure 9. As the viscous resistance coefficient decreased, the pressure distribution in the bearing clearance improved significantly.

The load carrying capacity of aerostatic bearings can be calculated by integrating the pressure distribution along the lower wall. The formula for this integration method is defined by the mathematical expression:

$$W = \int_0^{R_{\text{out}}} \int_0^{2\pi} PRd\theta dR, \quad (9)$$

Table 2 Detailed structural and material parameters of the three experimental samples

Design variable	Orifice restrictor	Multiple restrictors	Porous restrictors
Bearing diameter D /mm	50	50	50
Orifice diameter d /mm	0.0665	0.7	—
Groove width w_g /mm	—	0.20	—
Groove depth d_g /mm	—	0.10	—
Groove length l_g /mm	—	1.50	—
Viscous resistance coefficient d_v /m ⁻²	—	—	1.258×10^{14}
Inertia resistance coefficient c_i /m ⁻¹	—	—	2.498×10^7
Porosity γ	—	—	0.18

**Figure 4** Experimental setup for measuring the stiffness and stability of thrust pad aerostatic bearings

where W is the load capacity, P is the gas film pressure, R is the radius, R_{out} is the outer radius of the bearing clearance surface, and Θ is the angle in radians.

The load capacity of thrust pad aerostatic bearings with orifice restrictor is shown in Figure 10, from which it can be observed that bearing load capacity decreases with an increase in film thickness. With an increase of orifice restrictor diameter from 0.05 mm to 0.15 mm, the maximum load capacity improved from 105.6 N to 162.5 N. Compared to the orifice restrictor, the maximum load capacity of the multiple restrictors with diameters of 0.05, 0.10, and 0.15 mm increased significantly, to 259.4 N, 276.6 N, and 293.8 N, respectively, as shown in Figure 11. The simulation results show that the load capacity of a multiple restrictors is better than a single orifice restrictor. For the porous restrictors, the simulation results for load capacity are shown in Figure 12. The bearing load capacity decreased as the film thickness and the viscous resistance coefficient increased. The material parameters played a key role in the load capacity of thrust pad aerostatic bearings with porous restrictors. The maximum load capacity of the porous restrictors is close to that of the orifice restrictor but considerably lower than multiple restrictors.

The stiffness of thrust pad aerostatic bearings was determined by differentiating the bearing load capacity. The formula for this differential method is defined by the following mathematical expression:

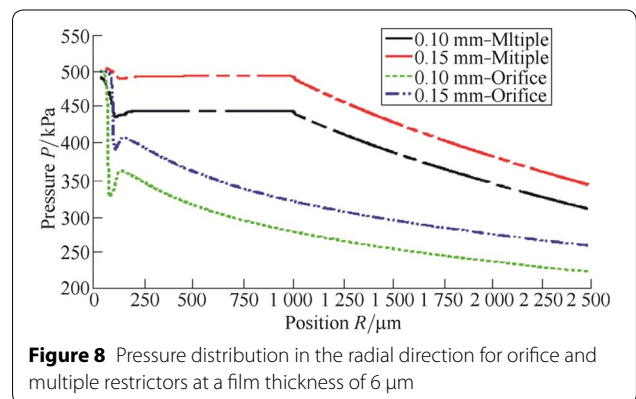
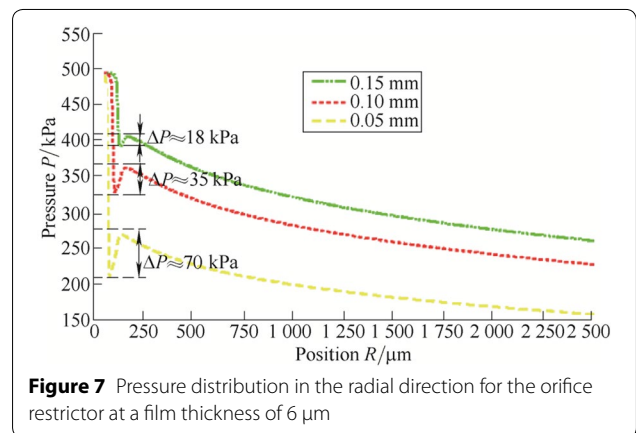
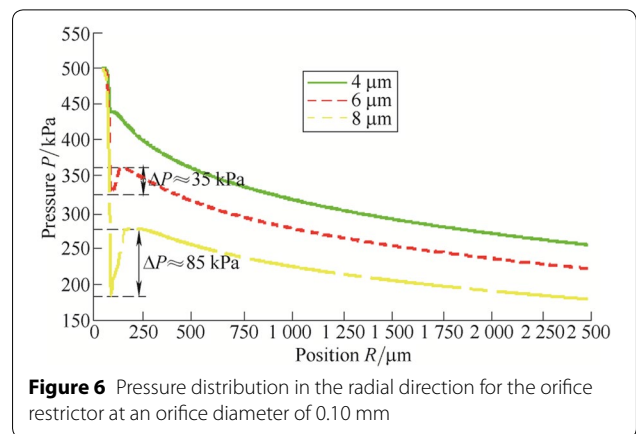
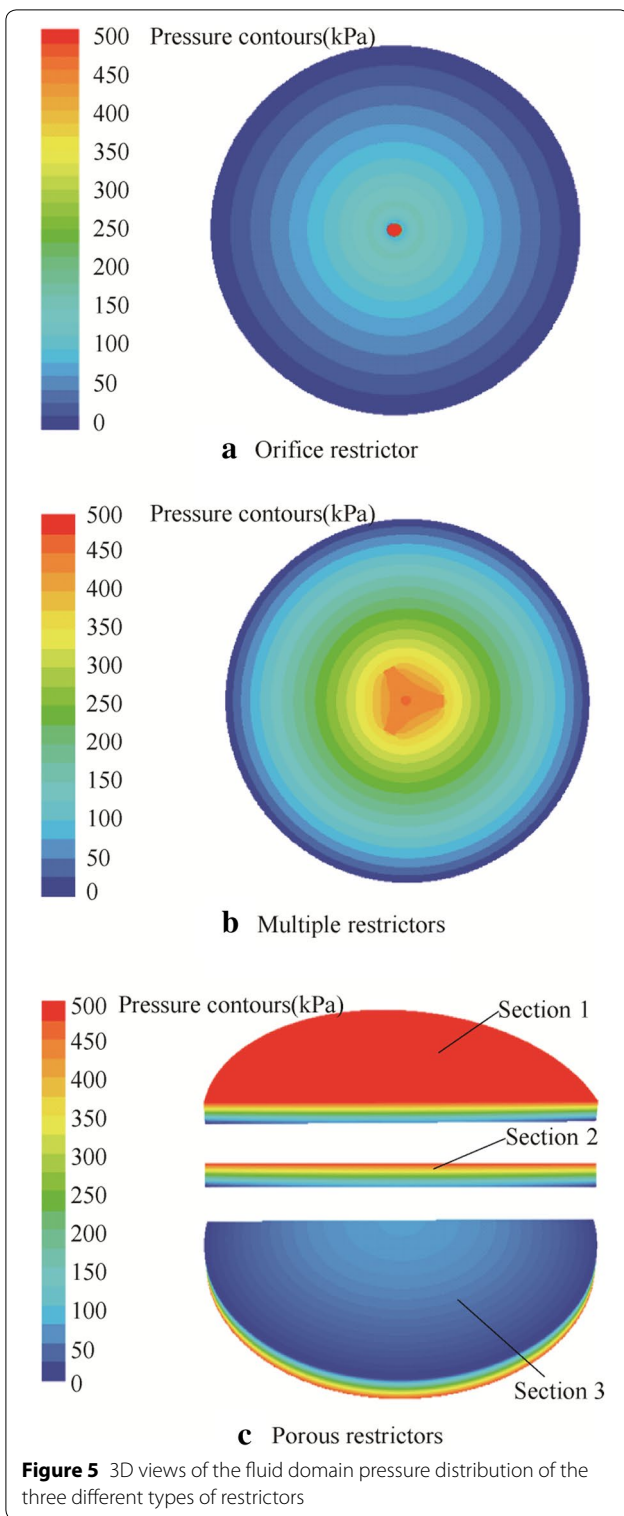
$$K = \lim_{\Delta h \rightarrow 0} \frac{W|_{h_0 - \Delta h} - W|_{h_0 + \Delta h}}{\Delta h}, \quad (10)$$

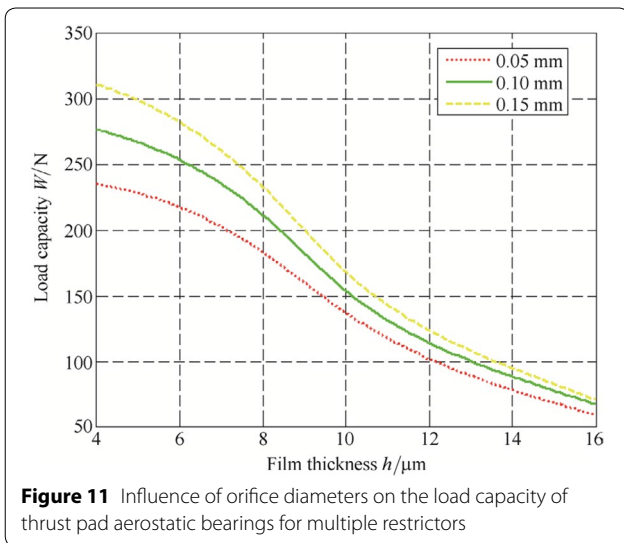
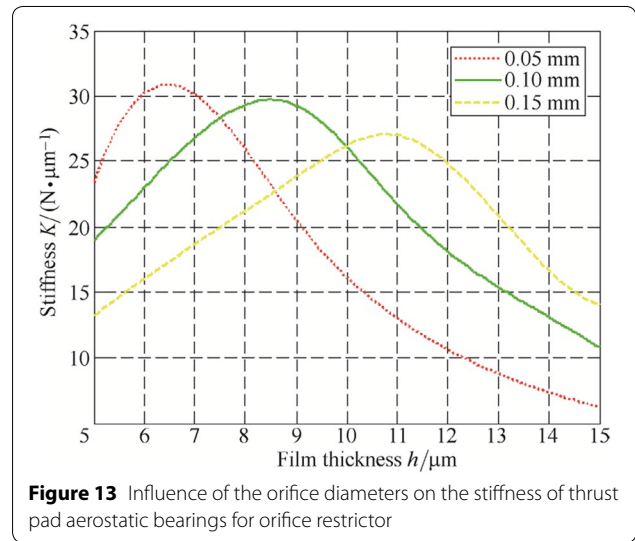
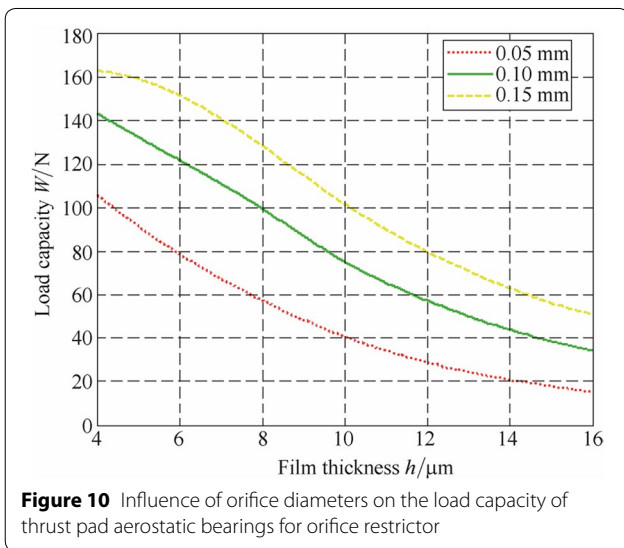
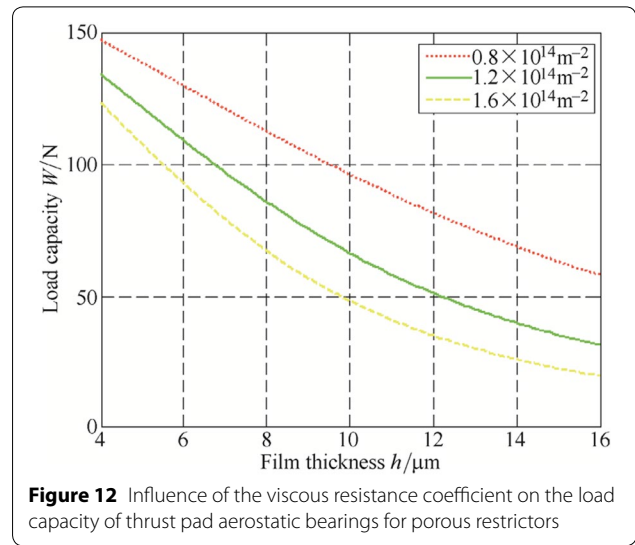
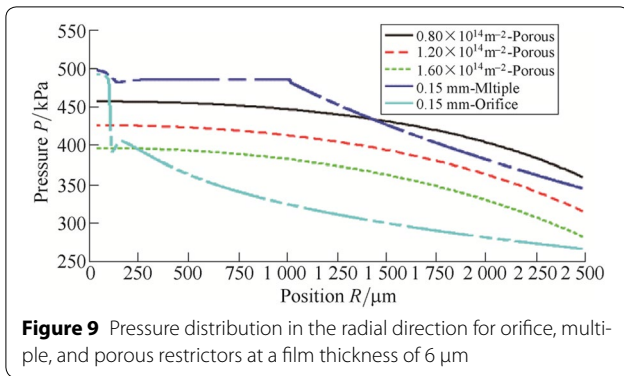
where K is the stiffness and h is the film thickness.

The stiffness of thrust pad aerostatic bearings with different types of restrictors is shown in Figures 13, 14, 15. The optimal stiffness of orifice restrictor with diameters of 0.05, 0.10, and 0.15 mm increases to 30.1 N/ μm , 29.2 N/ μm , and 26.9 N/ μm , and decreases at film thicknesses of 6.5 μm , 8.5 μm , and 11 μm , respectively. Compared to orifice restrictor, the optimal stiffness of multiple restrictors with diameters of 0.05, 0.10, and 0.15 mm increased to 69.6 N/ μm , 59.8 N/ μm , and 48.4 N/ μm , respectively. Figure 15 shows that the stiffness of the porous restrictors consistently increases with a decrease of the film thickness. Under the film thickness less than 8.5 μm , the stiffness increases with an increase of the viscous resistance coefficient. However, the stiffness behavior is reversed when the film thickness is greater than 11.5 μm . The maximum stiffness of the porous restrictors is also similar to that of the orifice restrictor but is considerably lower than that of the multiple restrictors.

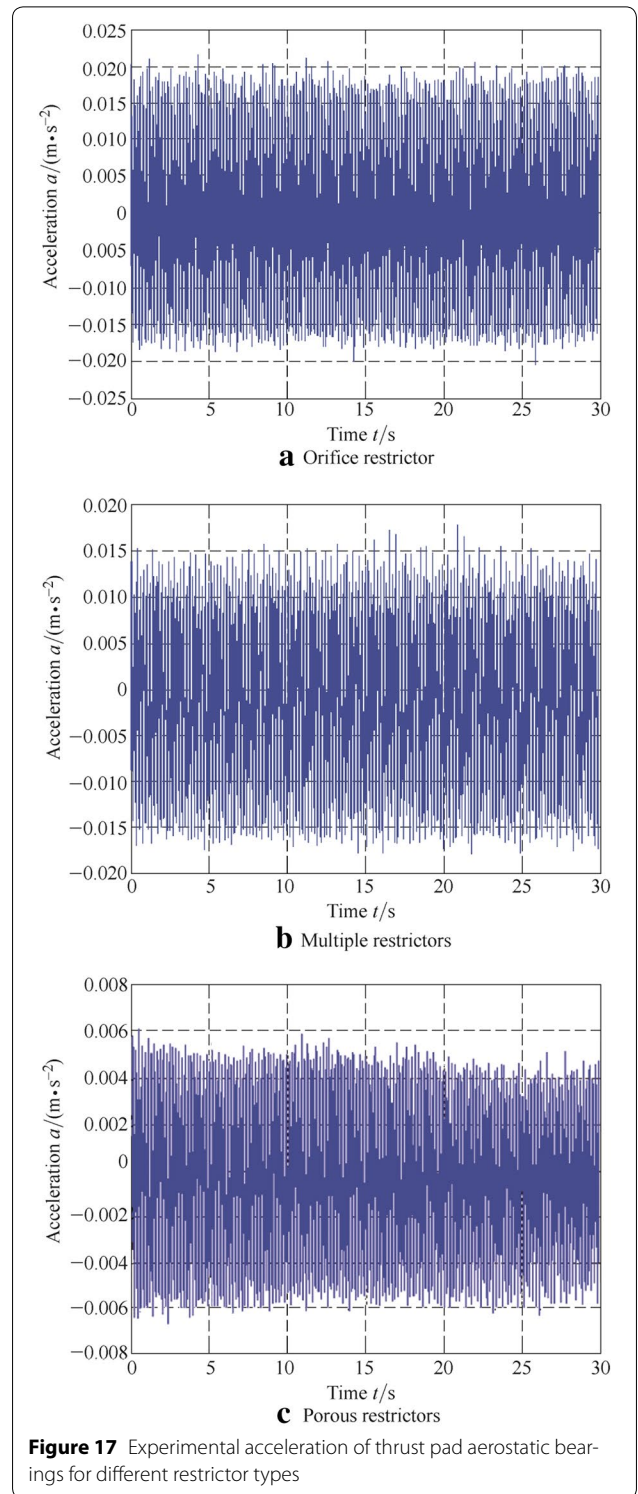
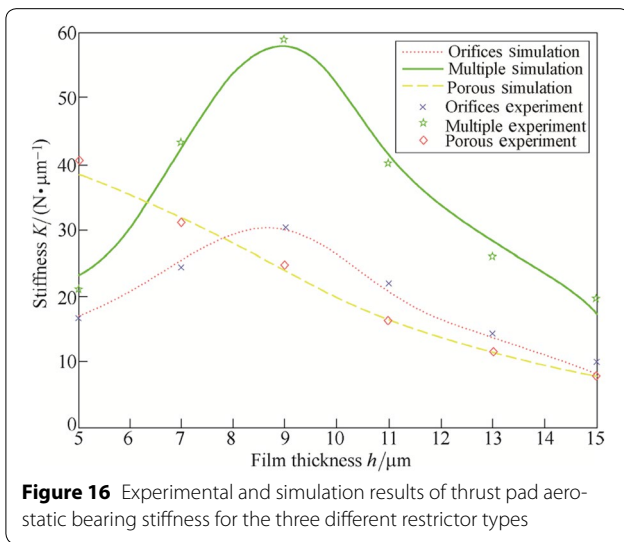
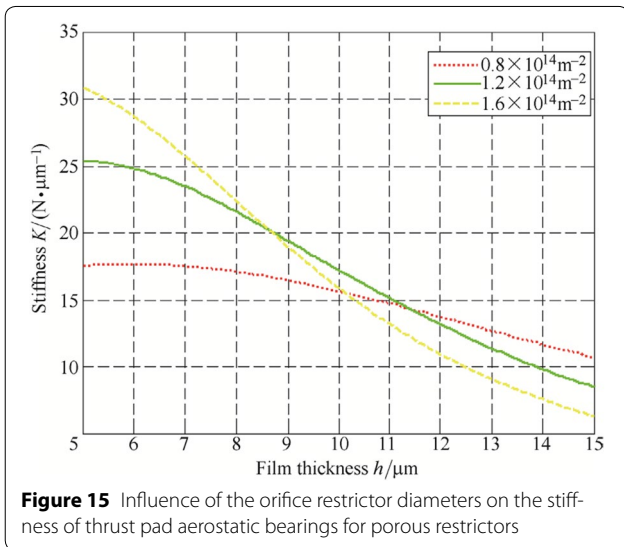
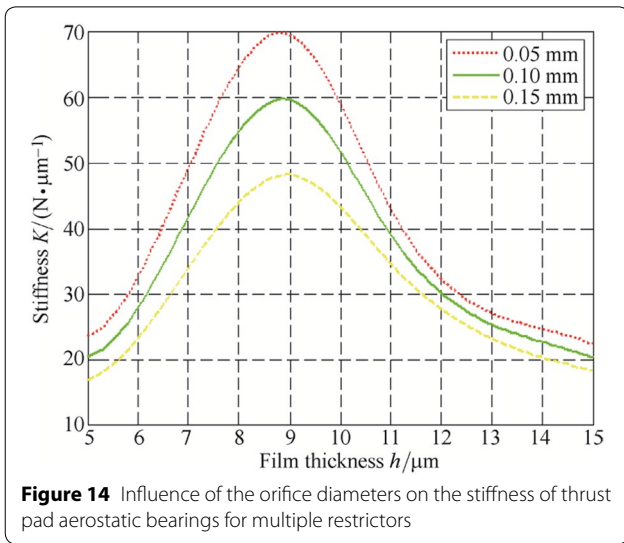
4.2 Experimental Verification

The experimental stiffness results of thrust pad aerostatic bearings with three different restrictor types are shown in Figure 16. The simulation results show good agreement with the experimental data, thus verifying the accuracy of the numerical simulation method used in this paper. The maximum difference between the experimental and numerical results with regard to stiffness was 11.02%. In Figure 16, the optimal stiffness of the multiple restrictors was significantly better than that of the orifice restrictor by 30.34 N/ μm . The porous restrictors was





clearly more advantageous when the film thickness was less than 6 μm. Relative to the orifice restrictor, which had an optimal stiffness of 15.71 N/μm, the optimal stiffness of the porous restrictors was significantly improved, with a value of 40.46 N/μm. Figure 17 shows the experimental acceleration of thrust pad aerostatic bearings with different types of restrictors. The micro-vibration of the multiple restrictors, with an acceleration of 0.015 m/s², was weaker than that of the orifice restrictor, which had an acceleration of 0.02 m/s², but was much stronger than that of the porous restrictors, which had an acceleration of 0.006 m/s².



5 Conclusions

- (1) The stiffness and stability of thrust pad aerostatic bearings are significantly influenced by the geometric and material parameters. For orifice restrictor and multiple restrictors, the stiffness gradually increases to a maximum and then decreases with an increase in film thickness. However, for porous restrictors, it consistently decreases.
- (2) The optimal stiffness of multiple restrictors is significantly better than that of the orifice restrictor, by 30.34 N/μm. The porous restrictors have a clear advantage at film thicknesses less than 6 μm. Compared to the orifice restrictor, the optimal stiffness of the porous restrictors can be improved from 15.71 N/μm to 40.46 N/μm.
- (3) The acceleration of the multiple restrictors, 0.015 m/s², is weaker than that of the orifice restrictor, 0.020 m/s², but is much stronger than that of the porous restrictors, which has a value of 0.006 m/s². This result demonstrates that the porous restrictors have better stability than the multiple restrictors and orifice restrictor.

Authors' Contributions

H-LC carried out the numerical simulation and manuscript writing. YW carried out the design and manufacture of restrictor. B-RW carried out the design and establishment of experiment platform. HY carried out the design and manufacture of thrust pad aerostatic bearings. HX carried out the analysis of experimental results and the revise of manuscript. All authors read and approved the final manuscript.

Authors' Information

Hai-Long Cui, born in 1989, is currently a PhD candidate and assistant professor at *Institute of Machinery Manufacturing Technology, China Academy of Engineering Physics*. He received his master degree from *University of Electronic Science and Technology, China*, in 2013. His research interests include design and manufacture of aerostatic bearing. Tel: +86-0816-2480487; E-mail: cuihai-long61@foxmail.com.

Yang Wang, born in 1963, is currently a professor a PhD candidate supervisor at *China Academy of Engineering Physics*. He received his PhD degree from *Northwestern Polytechnical University, China*, in 1999. His research interests include advanced optical manufacturing equipment technology. E-mail: wangyang@caep.com.

Bao-Rui Wang, born in 1961, is currently a professor and a PhD candidate supervisor at *Institute of Machinery Manufacturing Technology, China Academy of Engineering Physics*. He received his master degree from *Sichuan University, China*, in 1999. His research interests include advanced manufacturing technology. E-mail: wangbaorui@caep.com.

Hong Yang, born in 1985, is currently an assistant professor at *Institute of Machinery Manufacturing Technology, China Academy of Engineering Physics*. He received his PhD degree from *Sichuan University, China*, in 2012. His research interests include diamond cutting technology. E-mail: yanghong@caep.com.

Huan Xia, born in 1981, is currently an assistant professor at *Institute of Machinery Manufacturing Technology, China Academy of Engineering Physics*. He received his master degree from *China Academy of Engineering Physics, China*, in 2009. His research interests include precision and ultra-precision machining technology. E-mail: xiahuan@caep.com.

Competing Interests

The authors declare that they have no competing interests

Ethics Approval and Consent to Participate

Not applicable.

Funding

Supported by National Natural Science Foundation of China (Grant No. 51375325), NSAF (Grant Nos. U1530130), Shanxi coal based low carbon joint fund (U1610118), National Key Instrument Project (Grant No. 2016YFF0102003-02), Science Challenging Program of CAEP (Grant No. JCKY2016212A506-0106).

Publisher's Note

Springer Nature remains neutral with regard to jurisdictional claims in published maps and institutional affiliations.

Received: 14 April 2016 Accepted: 15 December 2016

Published online: 10 April 2018

References

- [1] D Huo, K Cheng, F Wardle. Design of a 5-axis ultraprecision micro milling machine—ultramill: part 1: holistic design approach, design considerations, and specifications. *International Journal of Advanced Manufacturing Technology*, 2010, 47: 867–877.
- [2] S Y Gao, K Cheng, H Ding. Multiphysics-based design and analysis of the high-speed aerostatic spindle with application to micro-milling. *Proceedings of the IMechE, Part J: Journal of Engineering Tribology*, 2016, 230(7): 852–871.
- [3] J L Yuan, F H Zhang, Y F Dai, et al. Development research of science and technologies in ultra-precision machining field. *Chinese Journal of Mechanical Engineering*, 2010, 46(8): 161–177. (in Chinese)
- [4] [W Wang, Z Jiang, W Tao, et al. A new test part to identify performance of five-axis machine tool—part I: geometrical and kinematic characteristics of S part. *International Journal of Advanced Manufacturing Technology*, 2015, 79:1–10.
- [5] C An, Y Zhang, Q Xu, et al. Modeling of dynamic characteristic of the aerostatic bearing spindle in an ultra-precision fly cutting machine. *International Journal of Machine Tools and Manufacture*, 2010, 50(4): 374–85.
- [6] S Y Gao, K Cheng, H Ding. CFD based investigation on influence of orifice chamber shapes for the design of aerostatic thrust bearings at ultra-high speed spindles. *Tribology International*, 2015, 92: 211–221.
- [7] Y Li, H Ding. Influences of the geometrical parameters of aerostatic thrust bearing with pocketed orifice-type restrictor on its performance. *Tribology International*, 2007, 40: 1120–1126.
- [8] J Renn, C Hsiao. Experimental and CFD study on the mass flow-rate characteristic of gas through orifice-type restrictor in aerostatic bearings. *Tribology International*, 2004, 37: 309–315.
- [9] K Cheng, W B Rowe. A selection strategy for the design of externally pressurized journal bearings. *Tribology International*, 1995, 28(7): 465–474.
- [10] Y S Chen, C C Chiu, Y D Cheng. Influences of operational conditions and geometric parameters on the stiffness of aerostatic journal bearings. *Precision Engineering*, 2010, 34: 722–734.
- [11] M T Neves, V A Schwarz, G J Menon. Discharge coefficient influence on the performance of aerostatic journal bearings. *Tribology International*, 2010, 43: 746–751.
- [12] J J Du, G Q Zhang, D Liu. Influences of pressure-equalizing groove on the load capacity of externally pressurized gas journal bearings. *Chinese Journal of Mechanical Engineering*, 2012, 48(8): 106–112. (in Chinese)
- [13] X D Chen, X M He. The effect of the recess shape on performance analysis of the gas-lubricated bearing in optical lithography. *Tribology International*, 2006, 39: 1336–1341.
- [14] N Bhat, S Kumar, W Tan. Performance of inherently compensated flat pad aerostatic bearings subject to dynamic perturbation forces. *Precision Engineering*, 2012, 36: 399–407.
- [15] U Nishio, K Somaya, S Yoshimoto. Numerical calculation and experimental verification of static and dynamic characteristic of aerostatic thrust bearings with small feedholes. *Tribology International*, 2011, 44: 1790–1795.

- [16] Z W Wang, A Sun. Research and development for supersonic phenomenon of externally pressure gas lubrication bearings. *Chinese Journal of Mechanical Engineering*, 2006, 42(1): 6–10. (in Chinese)
- [17] W L Xiong, Z Q Hou, L Lv. Study on the mechanism of hydrostatic spindle rotational error motion. *Chinese Journal of Mechanical Engineering*, 2014, 50(4): 112–119. (in Chinese)
- [18] X D Chen, H Chen, X Luo. Air vortices and nano-vibration of aerostatic bearings. *Tribology Letters*, 2011, 42(2): 179–183.
- [19] J C Zhu, H Chen, X D Chen. Large eddy simulation of vortex shedding and pressure fluctuation in aerostatic bearings. *Journal of Fluids and Structures* 2013, 40: 42–51.
- [20] E Mohamed. CFD investigation of pressure depressions in aerostatic circular thrust bearings. *Tribology International*, 2009, 42: 1108–1117.
- [21] S Yoshimoto, M Yamamoto, K Toda. Numerical calculations of pressure distribution in the bearing clearance of circular aerostatic thrust bearings with a single air supply inlet. *Transactions of the ASME*, 2007, 29: 384–390.
- [22] T H Panzera, J C Rubio, C R Bowen. Microstructural design of materials for aerostatic bearings. *Cement & Concrete Composites*, 2008, 30: 649–660.
- [23] Y Otsu, M Miyatake, S Yoshimoto. Dynamic characteristics of aerostatic porous journal bearings with a surface restricted layer. *Journal of Tribology*, 2011, 133(1): 186–192.
- [24] A Charki, K Diop, S Champmartin. Numerical simulation and experimental study of thrust air bearings with multiple orifice. *International Journal of Mechanical Sciences*, 2013, 72: 28–38.
- [25] J Huang, J H Zhang, W D Shi, et al. 3D FEM analyses on flow field characteristics of the valveless piezoelectric pump. *Chinese Journal of Mechanical Engineering*, 2016, 29(4): 825–831.
- [26] D H Wu, S Q Yuan, Y Ren, et al. CFD investigation of the influence of volute geometrical variations on hydrodynamic characteristics of circulator pump. *Chinese Journal of Mechanical Engineering*, 2016, 29(2): 315–324.
- [27] N Z Wang, C Y Chang, Y Tao. An application of Newton's method to the lubrication analysis of air-lubricated bearings. *Tribology Transactions*, 1999, 42(2): 419–424.

Submit your manuscript to a SpringerOpen[®] journal and benefit from:

- Convenient online submission
- Rigorous peer review
- Open access: articles freely available online
- High visibility within the field
- Retaining the copyright to your article

Submit your next manuscript at ► springeropen.com
